chemistry

MDPI

Article

Constructing a Triangle Ensemble of Pt Clusters for Enhanced Direct-Pathway Electrocatalysis of Formic Acid Oxidation

Cheng Li †, Zheng Tang †, Lanlan Shi, Yongjia Li, Yingjie Ji, Kaixin Zhang, Zhiyu Yang and Yi-Ming Yan *

State Key Lab of Organic-Inorganic Composites, Beijing Advanced Innovation Center for Soft Matter Science and Engineering, Beijing University of Chemical Technology, Beijing 100029, China

* Correspondence: yanym22@mail.buct.edu.cn

† These authors contributed equally to this work.

Abstract: The pursuit of operational advancements in direct formic acid fuel cells (DFAFCs) necessitates the development of high-performance platinum (Pt)-based catalysts for formic acid electrooxidation (FAOR). However, FAOR on Pt-based catalysts follows a dual pathway mechanism, in which the direct pathway is a preferred route due to its efficient dehydrogenation process. Conversely, the indirect pathway results in the generation of adsorbed CO species, a process that deleteriously poisons the active sites of the catalyst, with CO species only being oxidizable at higher potentials, causing a significant compromise in catalyst performance. Herein, we have successfully synthesized Pt-C_3N_4@CNT, where three Pt clusters are precisely dispersed in a triplet form within the C_3N_4 by virtue of the unique structure of C_3N_4. The mass activity for the direct pathway (0.44 V) delivered a current density of 1.91 A mg_{Pt}^{-1}, while the indirect pathway (0.86 V) had no obvious oxidation peak. The selectivity of Pt-C_3N_4@CNT catalysts for the direct pathway of FAOR was improved due to the special structure of C_3N_4, which facilitates the dispersion of Pt tri-atoms in the structure and the electronic interaction with Pt. In this study, we provide a new strategy for the development of highly active and selective catalysts for DFAFCs.

Keywords: formic acid; chemical anchoring; selectivity; direct pathway; fuel cell; atomic dispersion

check for updates

Citation: Li, C.; Tang, Z.; Shi, L.; Li, Y.; Ji, Y.; Zhang, K.; Yang, Z.; Yan, Y.-M. Constructing a Triangle Ensemble of Pt Clusters for Enhanced Direct-Pathway Electrocatalysis of Formic Acid Oxidation. *Chemistry* **2023**, *5*, 1621–1633. https://doi.org/10.3390/chemistry5030111

Academic Editor: Di Li

Received: 12 June 2023
Revised: 23 July 2023
Accepted: 24 July 2023
Published: 26 July 2023

1. Introduction

Formic acid oxidation reaction (FAOR) has been widely investigated with the development of direct formic acid fuel cells (DFAFCs) [1–6]. In addition, FAOR has been regarded as an ideal model reaction for exploring the structure–activity relationship of electrocatalysts and understanding the oxidation mechanism of more complex organics. The widely accepted dual-path mechanism of FAOR, as outlined in Scheme 1 [7–10], presents two distinctive pathways: The direct pathway proceeds via a dehydrogenation process forming a reactive intermediate (COOH*), which is subsequently oxidized to CO_2. In contrast, the indirect pathway generates adsorbed CO species (CO_{ads}) through a dehydration process, which can be oxidized to CO_2 at higher potentials. Despite the slow initial formation rate, CO_{ads} can accumulate on the Pt surface and significantly impede the direct pathway [11]. This presents a substantial challenge in the context of DFAFC applications, as the indirect pathway must be substantially suppressed to prevent the detrimental poisoning of active sites by the site-blocking CO_{ads} species, which in turn impedes the direct pathway of FAOR. To meet the requirements of practical applications, it is desirable to suppress the dehydration of formic acid, thus inhibiting the accumulation of CO_{ads}. Correspondingly, it is urgent to develop efficient catalysts by realizing the direct pathway of FAOR based on a deeper insight into the elementary steps of the mechanisms.

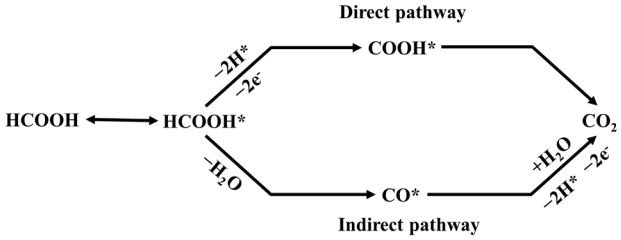

Scheme 1. Reaction mechanism of formic acid electrooxidation on the surface of Pt.

To date, several strategies have been employed in the design of catalysts aimed at modulating the FAOR reaction pathway on Pt-based catalysts. For instance, Pt alloys were prepared to alleviate the poisoning effect of CO_{ads} to improve the FAOR performance with a synergistic effect [12–14]. Moreover, the surface modification of Pt with organic molecules was proposed to inhibit the indirect pathway of FAOR [15–17]. Despite these achievements, an atomic-level understanding of the structure–activity relationship of Pt-based catalyst for FAOR is lacking. Atomic *ensemble effect*, i.e., modifying an adequate number of atoms in a suitable geometric arrangement at the catalyst surface, plays a crucial role of determining the reaction step, as well as the activity and/or selectivity of the catalyst [15,18]. Although a series of computational works have been contributed to investigate the atomic *ensemble effect* on the electrocatalytic reaction mechanisms, the experimental evidence based on the well-designing and preparation of the atomic ensemble of catalysts are seldomly reported. Recently, the advancements in confining ultrafine metal clusters provide good opportunities to manipulate the atomic ensemble of catalysts [19,20]. Therefore, it is possible to precisely prepare Pt-based ensembles to enhance the direct electrooxidation of formic acid by virtue of an *ensemble effect* and illuminate the reaction mechanism based on an explicit structure–activity relationship.

Herein, we report the construction of triangle clusters of Pt atoms by using graphitic carbon nitride as a structure-guiding template through the coordination between Pt and N atoms. The as-prepared Pt-C_3N_4@CNT showed promising activity for direct pathway FAOR with a mass activity of 1.91 A mg_{Pt}^{-1} at a peak potential of 0.44 V, which is significantly higher than that obtained on the Pt@CNT (0.11 A mg_{Pt}^{-1}). Besides, the j_d/j_i of Pt-C_3N_4@CNT is 10 times higher than that of Pt@CNT (j_d refers to the peak current density of direct pathway FAOR; j_i refers to the peak current density of indirect pathway FAOR). The single fuel cell device equipped with Pt-C_3N_4@CNT as an anodic catalyst was fabricated, delivering a high Pt mass power density (206.46 mW mg_{Pt}^{-1}), which is 4.8-fold higher than that obtained with Pt@CNT anodic catalyst (43.18 mW mg_{Pt}^{-1}). Moreover, mechanistic investigations show that the high activity and nearly complete direct pathway preference for FAOR obtained with Pt-C_3N_4@CNT can be attributed to the unique ensemble of Pt atoms, where the triangle clusters provide intimately adjacent Pt atoms for a direct dehydrogenation pathway.

2. Results and Discussion

Figure 1a illustrates the preparation procedure of Pt-C_3N_4@CNT catalyst. C_3N_4 was obtained by calcinating urea in a muffle furnace at 550 °C for 4 h. Then, C_3N_4, CNT, and $H_2PtCl_6 \cdot 6H_2O$ were dispersed in glycol and treated by co-heating at 160 °C for 3 h. Commonly, C_3N_4 has a graphene-like structure, except that it contains an internal triangle-shaped cavity with a side length of ≈0.72 nm. Such a unique structure offers an ideal platform for encapsulating the reactants in the internal triangle-shaped cavity [20]. Therefore, we intend to use C_3N_4 as a structure-guiding template to construct triangle clusters of single-atom Pt. On the one hand, the N sites exhibit a strong affinity for coordinating with Pt salt ions ($PtCl_4^{2-}$), thereby aiding the subsequent reduction to produce Pt atoms. On the other hand, the confined space in the cavity of C_3N_4 structure is believed to benefit the generation of isolated atoms. For comparison, a control sample (Pt@CNT) was prepared by following a similar process but without the addition of C_3N_4.

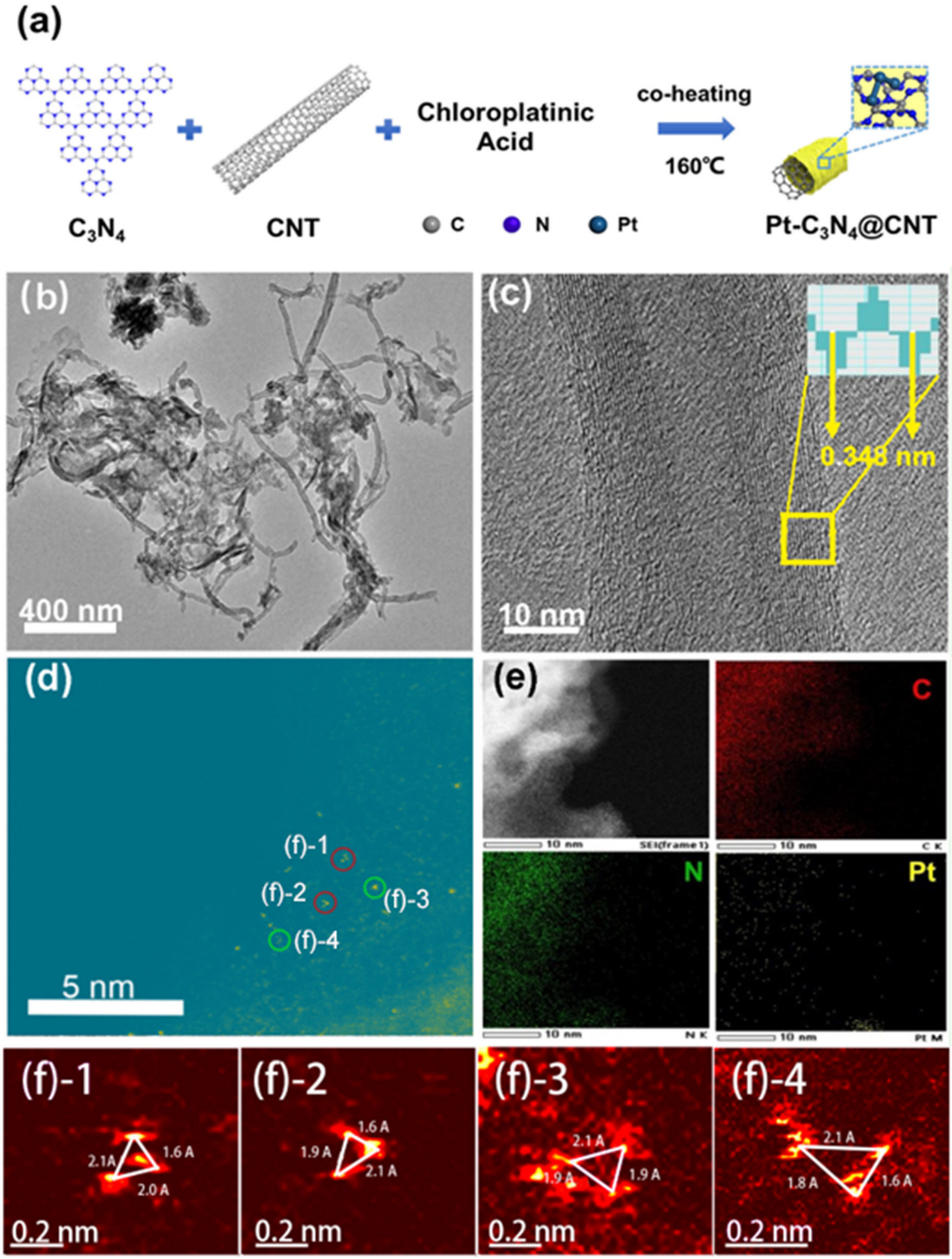

Figure 1. (**a**) Scheme for the synthesis of Pt-C_3N_4@CNT. (**b**) TEM images, (**c**) high-resolution TEM images, (**d**,**f**) HAADF-STEM images, and (**e**) EDS elemental mapping of Pt-C_3N_4@CNT.

Figure 1b,c show the transmission electron microscopy (TEM) and high-resolution TEM (HRTEM) images, respectively. TEM images confirm the obvious CNTs structure in Pt-C_3N_4@CNT, with typical hollow tubular morphology similar to pristine CNTs. Also, the CNTs structure of Pt@CNT was observed, as shown in Figure S1. For all samples, the morphology and structure of CNTs were well-maintained, indicating that the preparation

process did not change the pristine structure of CNTs. HRTEM images of Pt-C_3N_4@CNT, as depicted in Figure 1c, exhibit a typical graphitic structure of CNTs. Interestingly, a shell without distinct lattice fringes can be observed on the outer surface of the CNTs, which corresponds to the C_3N_4 shell. No obvious metallic lattice was observed in the Pt-C_3N_4@CNT, while there was a clear metallic lattice in the Pt@CNT structure identified as metallic Pt nanoparticles (Figure S2). The microstructure of the catalyst was further characterized by aberration-corrected high-angle annular dark-field scanning TEM (AC-HAADF-STEM). In the HAADF-STEM images of the Pt-C_3N_4@CNT sample (Figure 1d), evenly distributed bright spots are observed, indicative of the atomic dispersion of Pt. A particularly fascinating discovery is the significant proportion of atoms found in triangular clusters, in which three metal atoms closely associate with each other at an average distance of 0.17~0.25 nm (Figure 1f). This finding contrasts sharply with the control samples lacking C_3N_4 substrates, which exhibited conventional nanoparticle characteristics, alongside clearly visible lattice fringes of Pt upon further scrutiny (Figure S2). The geometry of this unique tri-metal atom matches nicely with the in-plane void of C_3N_4, which is triangle-shaped with a side length of ≈0.48 nm. This unique structure presents C_3N_4 with the capability to anchor metal atoms effectively, culminating in a tri-metal configuration that retains the distinctive triangular structure [20]. Moreover, energy-dispersive X-ray spectroscopy (EDX) analysis of Pt-C_3N_4@CNT revealed an even distribution of platinum, nitrogen, and carbon signals (Figure 1e), showcasing the uniform dispersion of C_3N_4 within the complex. Additionally, inductively coupled plasma atomic emission spectrometry (ICP-AES) was employed to evaluate the metal loadings in Pt-C_3N_4@CNT and Pt@CNT, which were found to be 1.76 wt% and 2.41 wt%, respectively. These results suggest that C_3N_4 offers an optimal class of templates for crafting such unique tri-metal atom structures. Such triangle clusters of Pt atoms could be highly favorable for FAOR.

The X-ray diffraction (XRD) patterns of both Pt-C_3N_4@CNT and Pt@CNT show the peaks which correspond to the CNT, and there are also peaks of C_3N_4 in Pt-C_3N_4@CNT, as shown in Figure 2a. However, there is no obvious peak of metallic Pt in the XRD pattern of Pt-C_3N_4@CNT, which indicates that there was no metal or metal compound formed in the sample. In contrast, there is an obvious peak of metallic Pt (PDF#65-2868) in the XRD patterns of Pt@CNT, thereby affirming that no metal or metal compounds materialized in Pt-C_3N_4@CNT. This conclusion aligns with the data procured from earlier HAADF-STEM imaging. Then, Raman spectroscopy and Fourier transform infrared (FTIR) spectroscopy were further performed to investigate the composition of the samples, as shown in Figure 2b,c, respectively. The Raman spectrum of the Pt-C_3N_4@CNT sample (Figure 2b) presents no notable peaks, attributable to the substantial presence of C_3N_4 in the material, thus the results largely mirror those of C_3N_4. In contrast, the Pt@CNT sample exhibits a Raman peak consistent with CNT [21,22]. Additionally, the D band (1360 cm^{-1}) and the G band (1600 cm^{-1}) appear in the Raman spectra, further confirming the presence of C_3N_4 in Pt-C_3N_4@CNT. The incorporation of C_3N_4 into Pt-C_3N_4@CNT is substantiated further through FTIR spectroscopy (Figure 2c). Peaks of the Pt-C_3N_4@CNT samples primarily occur at 811.3 cm^{-1}, between 1200 and 1700 cm^{-1}, and within 2800–3700 cm^{-1}, harmonizing with the characteristic peaks of C_3N_4. The peak at 811.3 cm^{-1} is linked to the stretching vibration of the triazine ring [23], whereas the peaks between 1200 and 1700 cm^{-1} correspond to the stretching pattern of aromatic carbon nitride heterocyclic units [24]. Specific peak assignments include 1247 cm^{-1} (stretching vibration of C–N(–C)–C or C–NH–C), 1312 cm^{-1} and 1637 cm^{-1} (stretching vibrations caused by C–N and C=N on the heterocyclic ring, respectively), and 1407 cm^{-1} (vibration of C=C bond). The broad peak from 3000 to 3600 cm^{-1} is attributed to vibrations caused by amine or hydroxyl groups [25]. In contrast, the Pt@CNT sample only exhibited a weak peak relating to CNT within the range of 3200–3700 cm^{-1} in the FTIR spectrum, with no characteristic peaks of C_3N_4 being detected. These findings strongly suggest the successful incorporation of C_3N_4 into Pt-C_3N_4@CNT. To further probe the surface chemical compositions of the resultant Pt-C_3N_4@CNT and Pt@CNT, X-ray photoelectron spectroscopy (XPS) was employed. The

Pt 4f spectrum (Figure 2d) of both Pt-C_3N_4@CNT and Pt@CNT reveal a distinct Pt 4f doublet assignable to the $4f_{5/2}$ and $4f_{7/2}$ peaks of Pt (0), corroborating the almost metallic nature of Pt in both configurations [26]. Nevertheless, on examining the precise peak positions of the two samples, a minor positive shift in the binding energy for Pt-C_3N_4@CNT was observed compared to Pt@CNT ($4f_{5/2}$: 73.65 eV for Pt-C_3N_4@CNT and 73.35 eV for Pt@CNT; $4f_{7/2}$: 70.35 eV for Pt-C_3N_4@CNT and 70.05 eV for Pt@CNT). This shift suggests a slight decrease in the electron density of Pt in the Pt-C_3N_4@CNT structure, potentially attributable to the presence of C_3N_4 [27]. The inferred electron transfer suggests that the minor reduction in surface electron density on Pt in Pt-C_3N_4@CNT could enhance its CO tolerance. Turning to the N 1s spectra of Pt-C_3N_4@CNT material (Figure 2e), the N 1s peak could be deconvoluted into four peaks of 398.8 eV, 399.8 eV, 401.3 eV, and 404.6 eV, which should be interpreted as C=N–C, tertiary nitrogen group ($(C)_3$–N), free amino group ($(C)_2$–NH, C–NH_2), and π excitations, respectively [28]. In contrast, the XPS spectra of Pt@CNT (Figure S5) display no N 1s peak, implying the absence of N elements. In the C 1s spectrum (Figure 2f) of Pt-C_3N_4@CNT, five peaks are discernible. Alongside the peaks at 287.5 eV, 284.8 eV, and 283.3 eV that are attributable to the CNT [29], two additional peaks at 286.8 eV (C–N=C) and 286.1 eV (C–N–C) can be traced back to two distinct carbon species within the basic aromatic CN heterocycles [30]. Contrastingly, only three peaks, all attributed to CNT, are present in the C 1s spectrum of Pt@CNT (Figure S6).

To test the electrochemical behaviors of the as-prepared samples, pristine samples were subjected to a cyclic voltammetry (CV) test in Ar-saturated 0.5 M H_2SO_4 solution. In order to investigate the effect of the Pt content on FAOR, samples with a different Pt content were evaluated through linear sweep voltammetry (LSV) tests (Figure S7). The Pt content was modulated at 1%, 2%, 3%, and 4%, with the respective samples being denoted as Pt-C_3N_4@CNT-1, Pt-C_3N_4@CNT-2, Pt-C_3N_4@CNT-3, and Pt-C_3N_4@CNT-4. As depicted in Figure S12, Pt-C_3N_4@CNT-2 exhibited the highest activity for FAOR via the direct pathway, thus denominated as Pt-C_3N_4@CNT. The Pt-C_3N_4@CNT and Pt@CNT samples showed different CV curves (Figures S11 and S12). Firstly, an absence of obvious underpotential deposition of hydrogen (H_{upd}) peaks was observed for Pt-C_3N_4@CNT, suggesting a dearth of Pt nanoparticles in this configuration. Secondly, the typical Pt–OH reduction peak, generally observed at approximately 0.65 V, was missing in the case of Pt-C_3N_4@CNT [31]. It is well-documented that H_{upd} would be formed on Pt of step, defect, and terrace sites. The lack of a H_{upd} peak on Pt-C_3N_4@CNT offers robust evidence corroborating the absence of Pt nanoparticles [31].

The FAOR performances of Pt-C_3N_4@CNT and Pt@CNT were explored in 0.5 M H_2SO_4 and 0.5 M HCOOH solutions. Figure 3a illustrates the superior performance of Pt-C_3N_4@CNT over Pt@CNT via anodic polarization, as evidenced by its elevated current density, particularly at lower potentials. It is noted that the anodic polarization profile of FAOR on Pt-based catalysts typically displays two peaks. The weaker peak at lower potential correlates to the oxidation of HCOOH to CO_2 via the direct pathway, while the stronger peak at a higher potential aligns with the oxidation of CO via the indirect pathway [32]. Furthermore, the anodic polarization curves of FAOR on Pt-C_3N_4@CNT and Pt@CNT were contrasted. The oxidation peak for CO_{ads} on Pt@CNT appears at ~0.86 V; a peak is nearly absent on Pt-C_3N_4@CNT. This suggests that FAOR primarily proceeds via the direct pathway on Pt-C_3N_4@CNT, underscoring its capacity as a highly active catalyst for FAOR with a strong predilection for the direct pathway. In addition, Cuesta et al. have also reported that the indirect pathway of FAOR to CO necessitates at least three linearly contiguous Pt atoms [33]. Consistent with this, experimental studies have shown that single-Pt-atom catalysts display no electrocatalytic FAOR current, implying that single-Pt-atom catalysts fall short for FAOR [6]. Maurer et al. carried out a comprehensive examination of single-atom platinum supported on CeO_2 [34], shedding light on the dynamic shifts induced during oxidation reactions and their implications for the activity of such catalytic systems. Their findings suggested that the initiation of CO oxidation is associated with the migration of platinum single sites from four-fold hollow sites to

form diminutive clusters comprising several platinum atoms [34]. These insights raise the prospect that single-atom catalysts might not necessarily provide the optimal structure for catalysis. In the context of Pt-C_3N_4@CNT catalyst, which features triangular clusters of Pt, the near-complete selectivity of the direct pathway for FAOR can be attributed to the presence of triads of Pt atoms within the structure. In order to demonstrate the results more visually, the mass activity and the specific activity of Pt-C_3N_4@CNT and Pt@CNT at 0.44 V were compared in the bar chart (Figure 3a). Compared with Pt@CNT, Pt-C_3N_4@CNT showed the highest mass activity of 1.91 A mg_{Pt}^{-1} and specific activity of 0.79 mA cm^{-2} at a potential of 0.44 V, signifying 17.4-fold and 2.6-fold enhancements relative to Pt@CNT (0.11 A mg_{Pt}^{-1} and 0.31 mA cm^{-2}), respectively. In addition, the current density of Pt-C_3N_4@CNT normalized by ECSA is 0.086 mA cm^{-2} mg, which is significantly higher than that of Pt@CNT (0.016 mA cm^{-2} mg). These results provide a compelling testament to the superior activity of Pt-C_3N_4@CNT as a catalyst for FAOR. Importantly, Pt-C_3N_4@CNT catalyst, structured with triangular clusters of Pt atoms, exhibited outstanding selectivity for the direct FAOR pathway, aligning with expectations. CVs of CNT (Figure S13), C_3N_4 (Figure S14), and C_3N_4@CNT (Figure S15) revealed an absence of FAOR current, thereby discounting the potential activity of CNT in FAOR. Furthermore, as shown in Figure S10, the mass activity of Pt@CNT is higher than that of Pt@CNT mixed with C_3N_4. The reason for this may be that the active site of Pt in Pt@CNT material is covered up after the addition of C_3N_4. Against this backdrop, we posit that the enhanced electrocatalytic performance of our catalysts can be chiefly attributed to the unique atomic dispersion structure of Pt-C_3N_4@CNT, which stabilizes the three-atom structure of the Pt cluster, forestalling aggregation into nanoparticles. This structural configuration amplifies catalytic activity and bolsters the utilization of precious metals [20]. Given the triangular clusters of Pt atoms within the Pt-C_3N_4@CNT catalyst, the near-total bias towards the direct pathway can be credited to the presence of two proximate Pt atoms in the Pt-C_3N_4@CNT structure.

To highlight the superior performance of the Pt-C_3N_4@CNT catalyst in formic acid electrooxidation, its catalytic activity was benchmarked against other Pt-based FOR catalysts, as documented in Table S1; the Pt-C_3N_4@CNT catalyst displayed both exceptional and comparable specific and mass activities when compared to other Pt-based catalysts. To further elucidate the resistance to poisoning exhibited by the two samples, a CO stripping experiment was undertaken. The CO stripping curves (Figure 3b,c) reveal the oxidation of adsorbed CO on Pt@CNT at 0.64 V, manifested as a prominent peak, which corroborates previous reports [35,36]. Intriguingly, Pt-C3N4@CNT displays only a minor peak at 0.61 V ascribed to the oxidation of adsorbed CO. The down-shift of the CO oxidation peak suggests an increased electron density on Pt, responsible for an enhancement of the back-donation of the platinum d orbital in the $2\pi^*$ antibonding orbital of CO, leading to a decrease in the Pt−CO bond strength [37]. Consequently, the triangular Pt clusters embedded within Pt-C3N4@CNT can curb the dehydration of formic acid and CO poisoning and promote the direct dehydrogenation pathway of formic acid [38,39]. To further appraise the resistance to poisoning of the two samples, CO gas was purposefully introduced into the electrolyte in the midst of chronoamperometry (CA) tests (Figure 3d) [40]. The relative reduction in mass activity of Pt-C_3N_4@CNT proved to be substantially less than that of Pt@CNT during CO introduction, thereby confirming the superior anti-poisoning ability of the Pt-C_3N_4@CNT catalyst. Furthermore, the morphology of Pt-C_3N_4@CNT has been preserved after stability tests verified by TEM and HRTEM images in Figures S3 and S4, demonstrating the good durability of Pt-C_3N_4@CNT.

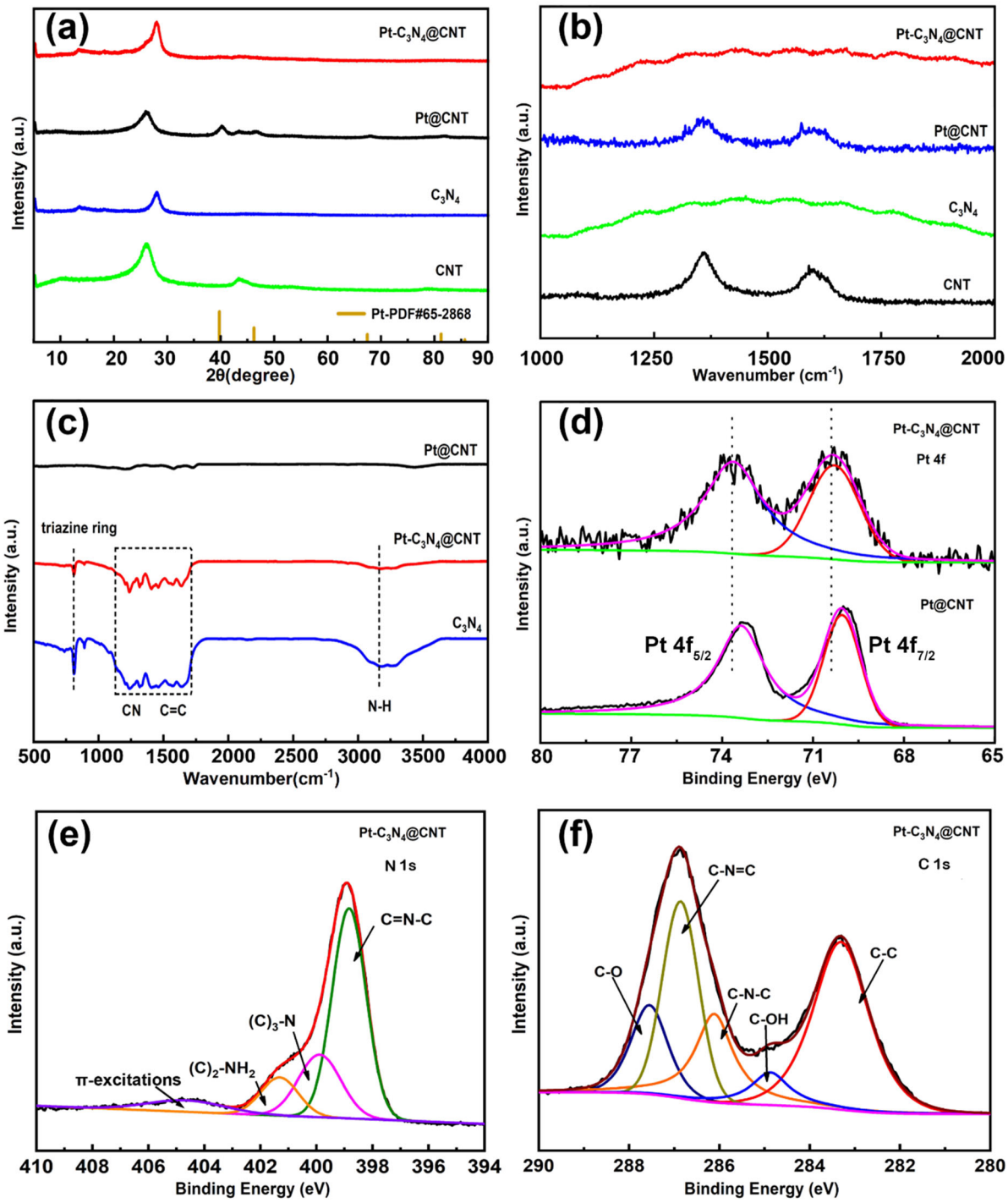

Figure 2. (**a**) XRD patterns of Pt−C_3N_4@CNT and Pt@CNT samples. (**b**) Raman spectra of Pt−C_3N_4@CNT and Pt@CNT samples. (**c**) FTIR spectra of Pt−C_3N_4@CNT and Pt@CNT samples. (**d**) Pt 4f XPS spectra of Pt−C_3N_4@CNT and Pt@CNT samples. XPS spectra of Pt−C_3N_4@CNT samples: (**e**) N 1s and (**f**) C 1s.

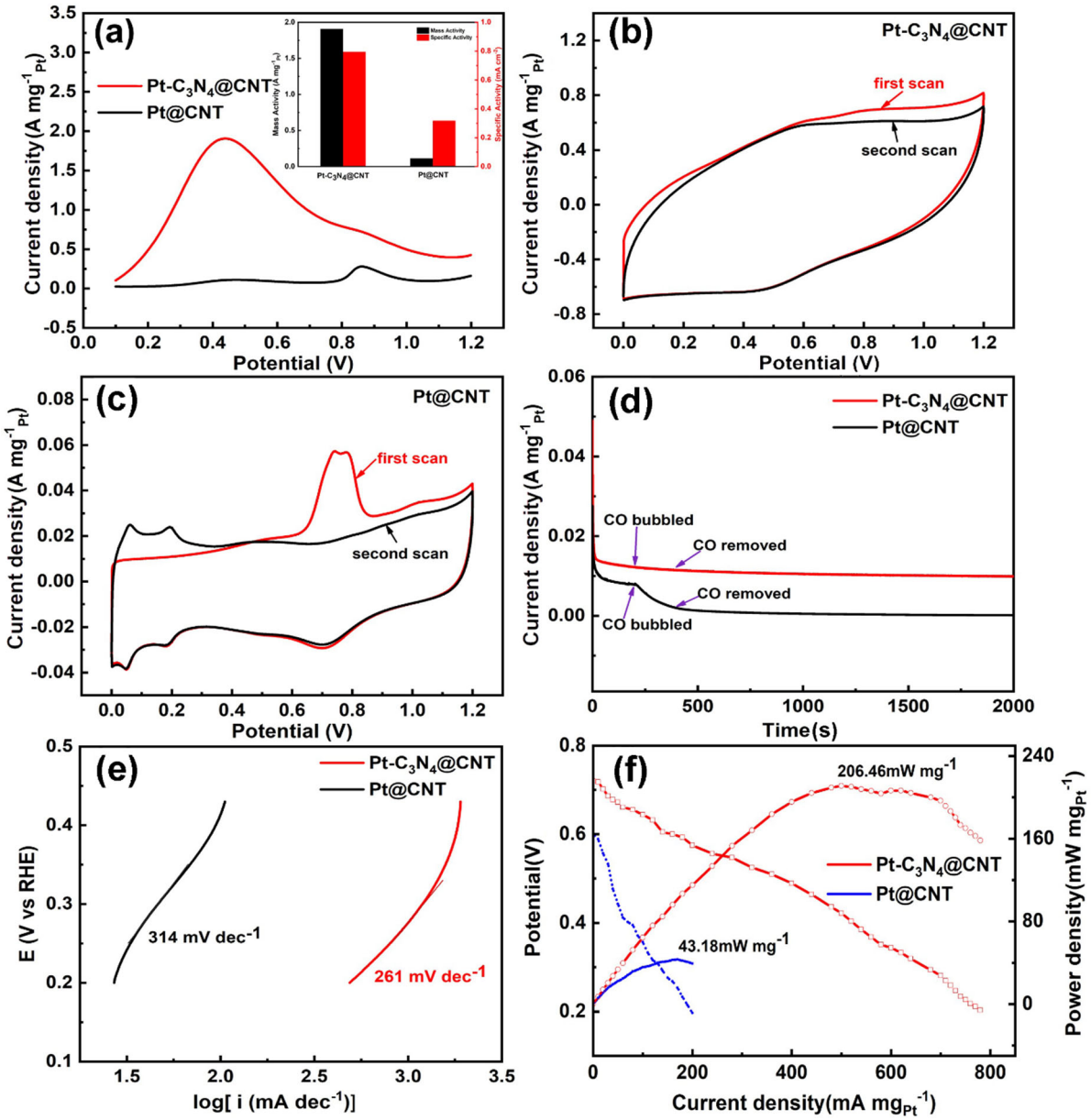

Figure 3. (**a**) Anodic polarization profiles of Pt−C_3N_4@CNT and Pt@CNT, and the insert shows the mass activity and specific activity of Pt−C_3N_4@CNT and Pt@CNT in 0.5 M H_2SO_4 + 0.5 M HCOOH. CO stripping of (**b**) Pt−C_3N_4@CNT and (**c**) Pt@CNT in 0.5 M H_2SO_4. All the potentials are vs. RHE. (**d**) CO poisoning experiment of Pt−C_3N_4@CNT and Pt@CNT in 0.5 M H_2SO_4 + 0.5 M HCOOH. Ar−rows serve to mark the instances where CO was introduced or extracted. (**e**) Tafel plots of Pt-C_3N_4@CNT and Pt@CNT. (**f**) Steady-state polarization and power density curves of Pt−C_3N_4@CNT and Pt@CNT for DFAFCs with formic acid (3 M) at 80 °C. The flow rate of formic acid is 3 mL min^{-1} and the flow rate of O_2 is 200 mL min^{-1}.

In addition, the electrochemical oxidation reaction kinetics of Pt-C_3N_4@CNT and Pt@CNT catalysts were studied using Tafel plots (Figure 3e). Notably, the Tafel plot for Pt-C_3N_4@CNT shows a smaller slope (261 mV dec^{-1}) than that of Pt@CNT (314 mV dec^{-1}) at lower potentials, suggesting that at these potentials, Pt-C_3N_4@CNT displays a predominant dehydrogenation pathway and a negligible dehydration pathway [41]. This smaller Tafel slope suggests that a lower overpotential is required to achieve the same current density, implying that Pt-C_3N_4@CNT can attain a higher catalytic current at the same overpotential and thus exhibits faster charge-transfer kinetics for formic acid oxidation

compared to Pt@CNT [42]. CO stripping experiments were also employed to estimate the electrochemically specific areas (ECSAs) of the two samples. The ECSAs of Pt-C_3N_4@CNT and Pt@CNT were found to be 240 m^2 g_{Pt}^{-1} and 35 m^2 g_{Pt}^{-1}, respectively. This indicates that the Pt-C_3N_4@CNT exposes a larger number of electrochemically active sites than Pt@CNT, further solidifying the superior electrocatalytic activity and predominant dehydrogenation pathway of Pt-C_3N_4@CNT in formic acid oxidation reaction. To further probe the intrinsic catalytic activity of the samples, the turnover frequency (TOF) of the catalysts during the FAOR was calculated. As depicted in Figure S16, Pt-C3N4@CNT exhibited a remarkably higher TOF of 1.88, compared to Pt@CNT (0.45).

To validate the exceptional performance of Pt-C_3N_4@CNT under practical operating conditions, single-cell tests were executed to holistically assess the electrochemical efficacy of the catalysts [43]. Employing Pt-C_3N_4@CNT and Pt@CNT as anodic catalysts and 60% Pt/C as cathodic catalysts for DFAFCs, Pt-C_3N_4@CNT exhibits a superior mass power density of 206.46 mW mg_{Pt}^{-1} (Figure 3f), marking a 4.8-fold increase over Pt@CNT at 80 °C (43.18 mW mg_{Pt}^{-1}). These observations indicate the promising potential of Pt-C_3N_4@CNT catalysts in DFAFCs.

DFT calculations were carried out to further elucidate the oxidation mechanism of formic acid on Pt-C_3N_4@CNT and Pt@CNT (Figure 4a,b). Figure 4c–f display the optimized structures of the intermediates in the two pathways. The Gibbs free energy profiles of formic acid oxidation (Figure 4a) unveil that the indirect oxidation pathway on Pt-C_3N_4@CNT spontaneously generates CO* + H_2O(l) from HCOOH*. However, the subsequent steps to form CO* + OH* from CO* + H_2O(l) and CO_2(g) from CO* + OH* are not thermodynamically favorable, exhibiting endothermic reaction energies of 0.61 eV and 1.24 eV, respectively. Hence, the production of CO_2(g) from CO* + OH* represents the rate-determining step. In the direct oxidation pathway, the formation of COOH* from HCOOH* requires only a nominal reaction energy of 0.11 eV. The subsequent conversion of COOH* to CO_2(g) is indeed endothermically, necessitating 1.04 eV of reaction energy. Despite being the rate-determining step, it still demands less energy than its equivalent in the indirect oxidation pathway. Consequently, from a thermodynamic standpoint, the direct oxidation route in Pt-C_3N_4@CNT offers a clear advantage over its indirect counterpart.

Based on the experimental observations and the calculated thermodynamic and kinetic data, we propose that the electrochemical oxidation of HCOOH on the Pt-C_3N_4@CNT surface predominantly follows the direct pathway, with COOH* as the preferred reactive intermediate, via:

$$\mathrm{HCOOH^*} \rightarrow \mathrm{COOH^*} + \mathrm{H^+} + \mathrm{e^-} \tag{1}$$

$$\mathrm{COOH^*} \rightarrow \mathrm{CO_2^*} + \mathrm{H^+} + \mathrm{e^-} \tag{2}$$

$$\mathrm{CO_2^*} \rightarrow \mathrm{CO_2(g)} \tag{3}$$

with the overall reaction:

$$\mathrm{HCOOH(g)} + * \rightarrow \mathrm{CO_2(g)} + * + 2\mathrm{H^+} + 2\mathrm{e^-} \tag{4}$$

Figure 4b highlights the Gibbs free energy curves for the direct pathways of the Pt-C_3N_4@CNT and Pt@CNT catalysts. Remarkably, the energy required for the adsorption of HCOOH(l) on Pt-C_3N_4@CNT is a mere 0.58 eV, significantly less than the 2.16 eV necessitated by Pt@CNT. This underlines that the formic acid oxidation on Pt-C_3N_4@CNT is thermodynamically more favorable.

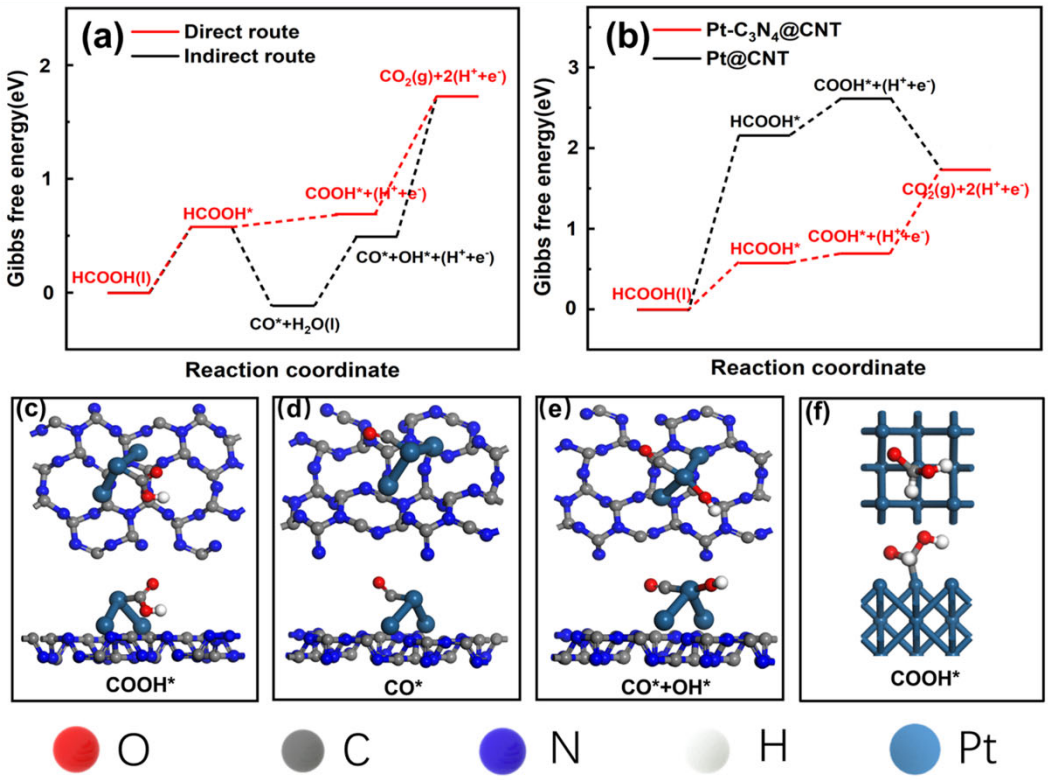

Figure 4. (**a**) Gibbs free energy profiles of formic acid oxidation via indirect and direct routes on the Pt-C_3N_4@CNT site. (**b**) Gibbs free energy profiles of formic acid oxidation via direct routes on the Pt-C_3N_4@CNT site and the @CNT site. (**c**–**e**) The optimized structures of the intermediates in the two routes on the Pt-C_3N_4@CNT site. (**f**) The optimized structures of the intermediates in the direct route on the Pt@CNT site.

3. Conclusions

In summary, we have successfully synthesized Pt-C_3N_4@CNT, equipped with triangular clusters of Pt atoms, serving as a high-performance anode electrocatalyst for DFAFCs. The as-prepared Pt-C_3N_4@CNT exhibits a high mass activity of 1.91 A mg_{Pt}^{-1} and an enhanced specific activity of 0.79 mA cm^{-2} at a potential of 0.44 V, which are 17.4- and 2.6-times higher than those of Pt@CNT (0.11 A mg_{Pt}^{-1} and 0.31 mA cm^{-2}), respectively. Importantly, we observed significantly weakened CO adsorption on the surface of Pt-C_3N_4@CNT, leading to its facile CO oxidation. Additional investigations employing single-cell tests with Pt-C_3N_4@CNT as the anode catalyst resulted in an enhanced mass power density of 206.46 mW mg_{Pt}^{-1}. DFT calculations further elucidated the mechanism of formic acid oxidation on Pt-C_3N_4@CNT, indicating a thermodynamic preference for a direct pathway. This nearly complete preference of a direct pathway for FAOR can be ascribed to the presence of adjacent Pt atoms in the Pt-C_3N_4@CNT. This study affirms the advantageous role of triangular Pt atom clusters for promoting the direct pathway for FAOR and underscores the unique contribution of the C_3N_4 structure in assembling these advantageous Pt clusters. These findings have substantial implications for the development of advanced DFAFCs, setting a new precedent for future explorations in the field.

Supplementary Materials: The following supporting information can be downloaded at: https://www.mdpi.com/article/10.3390/chemistry5030111/s1, Figure S1: TEM image of Pt@CNT; Figure S2: High-resolution TEM image of Pt@CNT; Figure S3: The TEM images of Pt-C_3N_4@CNT after stability tests; Figure S4: The HRTEM images of Pt-C_3N_4@CNT after stability tests; Figure S5: N 1s XPS spectrum of Pt@CNT; Figure S6: C 1s XPS spectrum of Pt@CNT; Figure S7: Anodic polarization profiles of Pt-C_3N_4@CNT obtained with different Pt content in 0.5 M H_2SO_4 + 0.5 M HCOOH. Scan rate: 50 mV s^{-1}; Figure S8: Anodic polarization profiles of Pt-C_3N_4@CNT and Pt@CNT, and shows

specific activity of Pt-C_3N_4@CNT and Pt@CNT iin 0.5 M H_2SO_4 + 0.5 M HCOOH; Figure S9: Anodic polarization profiles of Pt-C_3N_4@CNT and Pt@CNT, and shows the current density normalized through ECSA of Pt-C_3N_4@CNT and Pt@CNT iin 0.5 M H_2SO_4 + 0.5 M HCOOH; Figure S10: Anodic polarization profiles of the mass activity of Pt@CNT and Pt@CNT mixed with C_3N_4; Figure S11: CV curve of Pt-C_3N_4@CNT in 0.5 M H_2SO_4. Scan rate: 50 mV s^{-1}; Figure S12: CV curve of Pt@CNT in 0.5 M H_2SO_4 aqueous solution with the scan rate of 50 mV s^{-1}; Figure S13: CV curves f of CNT samples in 0.5 M H_2SO_4 aqueous solution (black), and in 0.5 M H_2SO_4 + 0.5 M HCOOH aqueous solution (red). Scan rate: 50 mV s^{-1}; Figure S14: CV curves f of C_3N_4 samples in 0.5 M H_2SO_4 aqueous solution (black), and in 0.5 M H_2SO_4 containing 0.5 M HCOOH aqueous solution (red). Scan rate: 50 mV s^{-1}; Figure S15: CV curves of C_3N_4@CNT samples in 0.5 M H2SO4 aqueous solution (black), and in 0.5 M H_2SO_4 + 0.5 M HCOOH aqueous solution (red). Scan rate: 50 mV s^{-1}; Figure S16: TOF of Pt-C_3N_4@CNT and Pt@CNT. Table S1: A literature survey of the catalytic activity of Pt-based FAOR catalysts. References [44–58] are cited in supplementary materials.

Author Contributions: Conceptualization, C.L., Z.Y. and Y.-M.Y.; formal analysis, Z.T., L.S., Y.L. and K.Z.; funding acquisition, Y.-M.Y.; investigation, C.L. and Y.-M.Y.; methodology, C.L., Z.Y. and Y.-M.Y.; resources, Y.-M.Y.; supervision, Z.Y. and Y.-M.Y.; visualization, Y.J.; writing—review and editing, Z.T., Y.L. and K.Z. All authors have read and agreed to the published version of the manuscript.

Funding: This research was funded by [Financial support from the National Natural Science Foundation of China] grant number [21575016, U20A20154] and the National Program for Support of Top-notch Young Professionals.

Data Availability Statement: Not applicable.

Acknowledgments: Financial support from the National Natural Science Foundation of China (grant nos. 21575016, U20A20154) and the National Program for Support of Top-notch Young Professionals is gratefully acknowledged.

Conflicts of Interest: The authors declare no conflict of interest.

References

1. Lai, J.; Niu, W.; Li, S.; Wu, F.; Luque, R.; Xu, G. Concave and duck web-like platinum nanopentagons with enhanced electrocatalytic properties for formic acid oxidation. *J. Mater. Chem. A* **2016**, *4*, 807–812. [CrossRef]
2. Vidal-Iglesias, F.J.; Lopez-Cudero, A.; Solla-Gullon, J.; Feliu, J.M. Towards more active and stable electrocatalysts for formic acid electrooxidation: Antimony-decorated octahedral platinum nanoparticles. *Angew. Chem. Int. Ed.* **2013**, *52*, 964–967. [CrossRef]
3. Su, N.; Chen, X.; Ren, Y.; Yue, B.; Wang, H.; Cai, W.; He, H. The facile synthesis of single crystalline palladium arrow-headed tripods and their application in formic acid electro-oxidation. *Chem. Commun.* **2015**, *51*, 7195–7198. [CrossRef] [PubMed]
4. Yang, S.; Dong, J.; Yao, Z.; Shen, C.; Shi, X.; Tian, Y.; Lin, S.; Zhang, X. One-pot synthesis of graphene-supported monodisperse Pd nanoparticles as catalyst for formic acid electro-oxidation. *Sci. Rep.* **2014**, *4*, 4501. [CrossRef]
5. Xiong, Y.; Dong, J.; Huang, Z.Q.; Xin, P.; Chen, W.; Wang, Y.; Li, Z.; Jin, Z.; Xing, W.; Zhuang, Z.; et al. Single-atom Rh/N-doped carbon electrocatalyst for formic acid oxidation. *Nat. Nanotechnol.* **2020**, *15*, 390–397. [CrossRef] [PubMed]
6. Li, Z.; Chen, Y.; Ji, S.; Tang, Y.; Chen, W.; Li, A.; Zhao, J.; Xiong, Y.; Wu, Y.; Gong, Y.; et al. Iridium single-atom catalyst on nitrogen-doped carbon for formic acid oxidation synthesized using a general host-guest strategy. *Nat. Chem.* **2020**, *12*, 764–772. [CrossRef]
7. Park, S.; Xie, Y.; Weaver, M.J. Electrocatalytic Pathways on Carbon-Supported Platinum Nanoparticles: Comparison of Particle-Size-Dependent Rates of Methanol, Formic Acid, and Formaldehyde Electrooxidation. *Langmuir* **2002**, *18*, 5792–5798. [CrossRef]
8. Zhong, W.H.; Wang, R.Y.; Zhang, D.J.; Liu, C.B. Theoretical Study of the Oxidation of Formic Acid on the PtAu(111) Surface in the Continuum Water Solution Phase. *J. Phys. Chem. C* **2012**, *116*, 24143–24150. [CrossRef]
9. Gao, W.; Song, E.H.; Jiang, Q.; Jacob, T. Revealing the active intermediates in the oxidation of formic acid on Au and Pt(111). *Chemistry* **2014**, *20*, 11005–11012. [CrossRef]
10. Xu, J.; Yuan, D.; Yang, F.; Mei, D.; Zhang, Z.; Chen, Y.X. On the mechanism of the direct pathway for formic acid oxidation at a Pt(111) electrode. *Phys. Chem. Chem. Phys.* **2013**, *15*, 4367–4376. [CrossRef]
11. Yue, C.M.Y.; Lim, K.H. Adsorption of Formic Acid and its Decomposed Intermediates on (100) Surfaces of Pt and Pd: A Density Functional Study. *Catal. Lett.* **2008**, *128*, 221–226. [CrossRef]
12. Geng, J.R.; Zhu, Z.; Bai, X.X.; Li, F.J.; Chen, J. Hot-Injection Synthesis of $PtCu_3$ Concave Nanocubes with High-Index Facets for Electrocatalytic Oxidation of Methanol and Formic Acid. *ACS Appl. Energy Mater.* **2020**, *3*, 1010–1016. [CrossRef]
13. Jiang, X.; Fu, G.; Wu, X.; Liu, Y.; Zhang, M.; Sun, D.; Xu, L.; Tang, Y. Ultrathin AgPt alloy nanowires as a high-performance electrocatalyst for formic acid oxidation. *Nano Res.* **2017**, *11*, 499–510. [CrossRef]
14. Scofield, M.E.; Koenigsmann, C.; Wang, L.; Liu, H.Q.; Wong, S.S. Tailoring the composition of ultrathin, ternary alloy PtRuFe nanowires for the methanol oxidation reaction and formic acid oxidation reaction. *Energ. Environ. Sci.* **2015**, *8*, 350–363. [CrossRef]

15. Gao, X.; Li, Y.; Zhang, Q.; Li, S.; Chen, Y.; Lee, J.-M. Polyethyleneimine-assisted synthesis of high-quality platinum/graphene hybrids: The effect of molecular weight on electrochemical properties. *J. Mater. Chem. A* **2015**, *3*, 12000–12004. [CrossRef]
16. Zhou, Z.Y.; Ren, J.; Kang, X.; Song, Y.; Sun, S.G.; Chen, S. Butylphenyl-functionalized Pt nanoparticles as CO-resistant electrocatalysts for formic acid oxidation. *Phys. Chem. Chem. Phys.* **2012**, *14*, 1412–1417. [CrossRef]
17. Zhou, X.; Liu, C.; Liao, J.; Lu, T.; Xing, W. Platinum-macrocycle co-catalysts for electro-oxidation of formic acid. *J. Power Sources* **2008**, *179*, 481–488. [CrossRef]
18. Jiang, K.; Zhang, H.X.; Zou, S.; Cai, W.B. Electrocatalysis of formic acid on palladium and platinum surfaces: From fundamental mechanisms to fuel cell applications. *Phys. Chem. Chem. Phys.* **2014**, *16*, 20360–20376. [CrossRef]
19. Yang, N.T.; Zhao, Y.H.; Wu, P.; Liu, G.J.; Sun, F.F.; Ma, J.Y.; Jiang, Z.; Sun, Y.H.; Zeng, G.F. Defective C_3N_4 frameworks coordinated diatomic copper catalyst: Towards mild oxidation of methane to C1 oxygenates. *Appl. Catal. B* **2021**, *299*, 120682. [CrossRef]
20. Wang, X.; Qiu, S.; Feng, J.; Tong, Y.; Zhou, F.; Li, Q.; Song, L.; Chen, S.; Wu, K.H.; Su, P.; et al. Confined Fe-Cu Clusters as Sub-Nanometer Reactors for Efficiently Regulating the Electrochemical Nitrogen Reduction Reaction. *Adv. Mater.* **2020**, *32*, e2004382. [CrossRef]
21. Bagchi, R.; Elshazly, M.; N'Diaye, J.; Yu, D.; Howe, J.Y.; Lian, K. Effects of Carboxyl Functionalized CNT on Electrochemical Behaviour of Polyluminol-CNT Composites. *Chemistry* **2022**, *4*, 1561–1575. [CrossRef]
22. Zhang, L.; Liang, J.; Yue, L.; Xu, Z.; Dong, K.; Liu, Q.; Luo, Y.; Li, T.; Cheng, X.; Cui, G.; et al. N-Doped Carbon Nanotubes Supported $CoSe_2$ Nanoparticles: A Highly Efficient and Stable Catalyst for H_2O_2 Electrosynthesis in Acidic Media. *Nano Res.* **2022**, *15*, 304–309. [CrossRef]
23. Han, Q.; Wang, B.; Gao, J.; Cheng, Z.; Zhao, Y.; Zhang, Z.; Qu, L. Atomically Thin Mesoporous Nanomesh of Graphitic C_3N_4 for High-Efficiency Photocatalytic Hydrogen Evolution. *ACS Nano* **2016**, *10*, 2745–2751. [CrossRef] [PubMed]
24. Dong, G.; Ai, Z.; Zhang, L. Efficient anoxic pollutant removal with oxygen functionalized graphitic carbon nitride under visible light. *RSC Adv.* **2014**, *4*, 5553. [CrossRef]
25. Li, J.; Shen, B.; Hong, Z.; Lin, B.; Gao, B.; Chen, Y. A facile approach to synthesize novel oxygen-doped g-C_3N_4 with superior visible-light photoreactivity. *Chem. Commun.* **2012**, *48*, 12017–12019. [CrossRef]
26. Zhang, L.; Long, R.; Zhang, Y.; Duan, D.; Xiong, Y.; Zhang, Y.; Bi, Y. Direct Observation of Dynamic Bond Evolution in Single-Atom Pt/C_3N_4 Catalysts. *Angew. Chem. Int. Ed.* **2020**, *59*, 6224–6229. [CrossRef] [PubMed]
27. Long, B.; Lin, J.; Wang, X. Thermally-induced desulfurization and conversion of guanidine thiocyanate into graphitic carbon nitride catalysts for hydrogen photosynthesis. *J. Mater. Chem. A* **2014**, *2*, 2942–2951. [CrossRef]
28. Liu, D.; Chen, D.; Li, N.; Xu, Q.; Li, H.; He, J.; Lu, J. Surface Engineering of g-C_3N_4 by Stacked BiOBr Sheets Rich in Oxygen Vacancies for Boosting Photocatalytic Performance. *Angew. Chem. Int. Ed.* **2020**, *59*, 4519–4524. [CrossRef]
29. Zhang, S.; Yang, Y.; Guo, Y.; Guo, W.; Wang, M.; Guo, Y.; Huo, M. Preparation and enhanced visible-light photocatalytic activity of graphitic carbon nitride/bismuth niobate heterojunctions. *J. Hazard. Mater.* **2013**, *261*, 235–245. [CrossRef]
30. Chen, K.; Chai, Z.; Li, C.; Shi, L.; Liu, M.; Xie, Q.; Zhang, Y.; Xu, D.; Manivannan, A.; Liu, Z. Catalyst-Free Growth of Three-Dimensional Graphene Flakes and Graphene/g-C_3N_4 Composite for Hydrocarbon Oxidation. *ACS Nano* **2016**, *10*, 3665–3673. [CrossRef]
31. Kim, J.; Roh, C.-W.; Sahoo, S.K.; Yang, S.; Bae, J.; Han, J.W.; Lee, H. Highly Durable Platinum Single-Atom Alloy Catalyst for Electrochemical Reactions. *Adv. Energy Mater.* **2018**, *8*, 1701476. [CrossRef]
32. Iyyamperumal, R.; Zhang, L.; Henkelman, G.; Crooks, R.M. Efficient electrocatalytic oxidation of formic acid using Au@Pt dendrimer-encapsulated nanoparticles. *J. Am. Chem. Soc.* **2013**, *135*, 5521–5524. [CrossRef] [PubMed]
33. Cuesta, A.; Escudero, M.; Lanova, B.; Baltruschat, H. Cyclic voltammetry, FTIRS, and DEMS study of the electrooxidation of carbon monoxide, formic acid, and methanol on cyanide-modified Pt(111) electrodes. *Langmuir* **2009**, *25*, 6500–6507. [CrossRef] [PubMed]
34. Maurer, F.; Jelic, J.; Wang, J.; Gänzler, A.; Dolcet, P.; Wöll, C.; Wang, Y.; Studt, F.; Casapu, M.; Grunwaldt, J.-D. Tracking the formation, fate and consequence for catalytic activity of Pt single sites on CeO_2. *Nat. Catal.* **2020**, *3*, 824–833. [CrossRef]
35. Intikhab, S.; Rebollar, L.; Li, Y.; Pai, R.; Kalra, V.; Tang, M.H.; Snyder, J.D. Caffeinated Interfaces Enhance Alkaline Hydrogen Electrocatalysis. *ACS Catal.* **2020**, *10*, 6798–6802. [CrossRef]
36. Zhang, S.; Shao, Y.; Yin, G.; Lin, Y. Electrostatic self-assembly of a Pt-around-Au nanocomposite with high activity towards formic acid oxidation. *Angew. Chem. Int. Ed.* **2010**, *49*, 2211–2214. [CrossRef]
37. Ma, J.; Habrioux, A.; Morais, C.; Lewera, A.; Vogel, W.; Verde-Gómez, Y.; Ramos-Sanchez, G.; Balbuena, P.B.; Alonso-Vante, N. Spectroelectrochemical Probing of the Strong Interaction between Platinum Nanoparticles and Graphitic Domains of Carbon. *ACS Catal.* **2013**, *3*, 1940–1950. [CrossRef]
38. Hammer, B.; Nielsen, O.H.; Nrskov, J.K. Structure sensitivity in adsorption: CO interaction with stepped and reconstructed Pt surfaces. *Catal. Lett.* **1997**, *46*, 31–35. [CrossRef]
39. Kitchin, J.R.; Norskov, J.K.; Barteau, M.A.; Chen, J.G. Role of strain and ligand effects in the modification of the electronic and chemical properties of bimetallic surfaces. *Phys. Rev. Lett.* **2004**, *93*, 156801. [CrossRef]
40. Huang, W.; Wang, H.; Zhou, J.; Wang, J.; Duchesne, P.N.; Muir, D.; Zhang, P.; Han, N.; Zhao, F.; Zeng, M.; et al. Highly active and durable methanol oxidation electrocatalyst based on the synergy of platinum-nickel hydroxide-graphene. *Nat. Commun.* **2015**, *6*, 10035. [CrossRef]

41. Uwitonze, N.; Zhou, D.; Lei, J.; Chen, W.; Zuo, X.Q.; Cai, J.; Chen, Y.-X. The high Tafel slope and small potential dependence of activation energy for formic acid oxidation on a Pd electrode. *Electrochim. Acta* **2018**, *283*, 1213–1222. [CrossRef]
42. Wang, Y.; Wu, B.; Gao, Y.; Tang, Y.; Lu, T.; Xing, W.; Liu, C. Kinetic study of formic acid oxidation on carbon supported Pd electrocatalyst. *J. Power Sources* **2009**, *192*, 372–375. [CrossRef]
43. Liu, Q.; Liu, X.; Zheng, L.; Shui, J. The Solid-Phase Synthesis of an Fe-N-C Electrocatalyst for High-Power Proton-Exchange Membrane Fuel Cells. *Angew. Chem. Int. Ed.* **2018**, *57*, 1204–1208. [CrossRef] [PubMed]
44. Kresse, G.; Furthmüller, J. Efficiency of ab-initio total energy calculations for metals and semiconductors using a plane-wave basis set. *Comput. Mater. Sci.* **1996**, *6*, 15–50. [CrossRef]
45. Kresse, G.; Furthmuller, J. Efficient iterative schemes for ab initio total-energy calculations using a plane-wave basis set. *Phys. Rev. B* **1996**, *54*, 11169–11186. [CrossRef]
46. Perdew, J.P.; Burke, K.; Ernzerhof, M. Generalized Gradient Approximation Made Simple. *Phys. Rev. Lett.* **1996**, *77*, 3865–3868. [CrossRef]
47. Kresse, G.; Joubert, D. From ultrasoft pseudopotentials to the projector augmented-wave method. *Phys. Rev. B* **1999**, *59*, 1758–1775. [CrossRef]
48. Blochl, P.E. Projector augmented-wave method. *Phys. Rev. B* **1994**, *50*, 17953–17979. [CrossRef]
49. Fu, X.; Li, H.; Xu, A.; Xia, F.; Zhang, L.; Zhang, J.; Ma, D.; Wu, J.; Yue, Q.; Yang, X.; et al. Phase Engineering of Intermetallic $PtBi_2$ Nanoplates for Formic Acid Electrochemical Oxidation. *Nano Lett.* **2023**, *23*, 5467–5474. [CrossRef]
50. Shi, H.; Liao, F.; Zhu, W.; Shao, C.; Shao, M. Effective PtAu Nanowire Network Catalysts with Ultralow Pt Content for Formic Acid Oxidation and Methanol Oxidation. *Int. J. Hydrogen Energy* **2020**, *45*, 16071–16079. [CrossRef]
51. Luo, S.; Chen, W.; Cheng, Y.; Song, X.; Wu, Q.; Li, L.; Wu, X.; Wu, T.; Li, M.; Yang, Q.; et al. Trimetallic Synergy in Intermetallic PtSnBi Nanoplates Boosts Formic Acid Oxidation. *Adv. Mater.* **2019**, *31*, 1903683. [CrossRef] [PubMed]
52. Tang, M.; Chen, W.; Luo, S.; Wu, X.; Fan, X.; Liao, Y.; Song, X.; Cheng, Y.; Li, L.; Tan, L.; et al. Trace Pd Modified Intermetallic PtBi Nanoplates towards Efficient Formic Acid Electrocatalysis. *J. Mater. Chem. A* **2021**, *9*, 9602–9608. [CrossRef]
53. Li, X.; Sun, Y.; Shen, C.; Zheng, Z.; Chen, H.; Jiang, Y.; Xie, Z. Heterogeneous fcc-Pt/hcp-PtBi Thick-Edge Nanoplates with Enhanced Activity for Formic Acid Oxidation. *ACS Appl. Energy Mater.* **2021**, *4*, 9190–9197. [CrossRef]
54. Kang, Y.; Qi, L.; Li, M.; Diaz, R.E.; Su, D.; Adzic, R.R.; Stach, E.; Li, J.; Murray, C.B. Highly Active Pt_3Pb and Core–Shell Pt_3Pb–Pt Electrocatalysts for Formic Acid Oxidation. *ACS Nano* **2012**, *6*, 2818–2825. [CrossRef] [PubMed]
55. Zhang, S.; Shao, Y.; Yin, G.; Lin, Y. Facile Synthesis of PtAu Alloy Nanoparticles with High Activity for Formic Acid Oxidation. *J. Power Sources* **2010**, *195*, 1103–1106. [CrossRef]
56. Liang, M.; Xia, T.; Gao, H.; Zhao, K.; Cao, T.; Deng, M.; Ren, X.; Li, S.; Guo, H.; Wang, R. Modulating Reaction Pathways of Formic Acid Oxidation for Optimized Electrocatalytic Performance of PtAu/CoNC. *Nano Res.* **2022**, *15*, 1221–1229. [CrossRef]
57. Xia, B.Y.; Wu, H.B.; Yan, Y.; Lou, X.W.; Wang, X. Ultrathin and Ultralong Single-Crystal Platinum Nanowire Assemblies with Highly Stable Electrocatalytic Activity. *J. Am. Chem. Soc.* **2013**, *135*, 9480–9485. [CrossRef]
58. Kim, Y.J.; Lee, H.; Chung, H.-S.; Sohn, Y.; Rhee, C.K. Pt-Bi Co-Deposit Shell on Au Nanoparticle Core: High Performance and Long Durability for Formic Acid Oxidation. *Catalysts* **2021**, *11*, 1049. [CrossRef]